



# Numerical study of interface cracking in composite structures using a novel geometrically nonlinear Linear Elastic Brittle Interface Model: Mixed-mode fracture conditions and application to structured interfaces

L. García-Guzmán<sup>a</sup>, J. Reinoso<sup>a,\*</sup>, A. Valderde-González<sup>a,b</sup>, E. Martínez-Pañeda<sup>c</sup>, L. Távora<sup>a</sup>

<sup>a</sup> Grupo de Elasticidad y Resistencia de Materiales, Escuela Técnica Superior de Ingeniería, Universidad de Sevilla, Camino de los Descubrimientos s/n, 41092 Sevilla, Spain

<sup>b</sup> IMT School for Advanced Studies, Piazza San Francesco 19, Lucca 55100, Italy

<sup>c</sup> Department of Civil and Environmental Engineering, Imperial College London, London SW7 2AZ, UK

## ARTICLE INFO

### Keywords:

Structured interfaces  
Interface cracking  
LEBIM  
Fracture toughness  
Mixed-mode

## ABSTRACT

Interface cracking is one of the most prominent failure modes in fibre reinforced polymer (FRP) composites. Recent trends in high-tech applications of FRP composites exploit the limits of the load bearing capacity, generally encompassing the development of notable nonlinear effects from geometrical and material signatures. In this investigation, we present a comprehensive assessment of the new Linear Elastic Brittle Interface Model (LEBIM) in geometrically nonlinear applications undergoing mixed-mode fracture conditions. This interface model for triggering fracture events is formulated through the advocacy of continuum-like assumptions (for initial non-zero interface thickness) and allows the incorporation of the potential role of in-plane deformation effects. The performance of the present interface model is demonstrated through the simulation of specimens with mixed-mode delamination, with special attention to its application in samples equipped with structured interfaces. Predictions exhibit an excellent agreement with experimental data, validating the proposed methodology.

## 1. Introduction

The recurrent requirements for the achievement of high strength-to-weight ratios in different engineering applications have led to the continuous improvement of production techniques and methodologies of analysis. In this direction, fibre reinforced polymers (FRP) composite materials have become particularly popular relative to conventional materials (especially in contrast to metals) due to their appealing strength and stiffness, widening the current ranges of applicability within the aerospace, automotive or renewable industries, among other sectors.

However, the inherent heterogeneous character of FRP composites at several scales of observation entails characteristic failure phenomena between the composing entities and the constituents. This is the case, for instance, of delamination events at the macro-scale [1–3] and fibre-matrix debonding [4,5] at the micro-scale, among many other debonding-like failures in FRP composites. Such cracking events can be principally caused either by external loading actions or induced by manufacturing and joining processes [6]. Motivated by these failure phenomena, significant research efforts have been conducted in recent

years towards the efficient incorporation of alternative joining procedures; such as adhesive bonding, a compelling technique that provides additional advantages in terms of the mechanical responses in conjunction with the enhancement of fatigue and environmental performances [7].

The understanding of failure mechanisms in solids, with special interest on joints/interfaces, has been of high interest in both industrial and research contexts, striving for the development of different prediction methodologies. Thus, on the one hand, the Linear Elastic Fracture Mechanics (LEFM) approach, relying on its energetic version, makes use of an energy criterion to predict failure either in the adherents, the adhesive or the interface between them. The energy-based LEFM was originally proposed by Griffith [8] and posteriorly revisited by Irwin [9]. One of the most popular LEFM-based methodologies is the so-called Virtual Crack Closure Technique (VCCT), where the crack advance is triggered as long as the energy release rate exceeds a certain threshold or critical value under pure or mixed-mode fracture conditions [10]. In this regard, studies of the stress intensity factors for homogeneous and multi-material specimens have been comprehensively addressed in [11–14] in order to determine proper conditions

\* Corresponding author.

E-mail address: [jreinoso@us.es](mailto:jreinoso@us.es) (J. Reinoso).

for fracture progression, whereas the extension on the application of Fracture Mechanics to nonlinear materials was conducted by Rice and co-authors through the so-called J-Integral method [15].

Alternatively to fracture mechanics-based methods, a different perspective for predicting the fracture response in solids can be advocated by means of Cohesive Zone Model (CZM) techniques, which have been extensively used for triggering interface fracture phenomena [16]. Originally proposed by Barenblatt [17] and Dugdale [18], CZMs are generally formulated within the context of Damage Mechanics of irreversible processes [19,20]. Thus, in the particular case of interface fracture, the scalar-based damage variable within the CZ formulation accounts for the stiffness degradation within the so-called fracture process zone (FPZ) obeying the particular form of the traction-separation law (TSL). This TSL relates the displacement jumps across the interface with the respective traction components [21]. The flexibility of CZMs in terms of the TSL definition (featuring bilinear [22], trapezoidal [23], exponential [24] laws, among many others) permits the characterization of different adhesives or interfaces, whilst the proper parameters of the cohesive zone can be extracted from experimental data as proposed in [25,26].

An interesting approach in interface fracture mechanics is endowed through the consideration of the interface/joint as a continuous distribution of linear springs. This interface formulation, usually denominated as Linear Elastic-Brittle Interface Model (LEBIM), encompasses a linear elastic relationship between the displacement jumps and the corresponding tractions across the interface up to abrupt failure, which is tracked once a particular fracture criterion is violated. This methodology was proposed by Prandtl [27] and Mott [28], and it is mainly suitable for scenarios where the overall stiffness is ruled by the adherents, and the gradual stiffness loss due to the interface degradation can be neglected. Thus, this interface conception has been efficiently used to represent the behaviour of brittle-like interfaces, such as epoxy-based adhesives [3,7,29,30].

Another key aspect for accurate predictions within the context of interface/joint fracture concerns the rigorous selection of the kinematic hypotheses in accordance with the experimental conditions. That is, whether material and geometrical nonlinearities concomitantly evolve throughout the numerical analysis. This aspect has a direct reflection on the way through which the stress and strain fields are computed, and therefore determine the onset and propagation of failure. In many lightweight structures, such as those extensively used in aerospace or renewable industry (e.g., stiffened panels and turbine blades, among many other), high-performance materials permit the evolution of large displacements during the loading applications prior to reaching the corresponding collapsing points. A principal after-effect is the non-negligible difference between original and current configurations, that leads to inaccurate calculations if the analysis is restricted to small-displacement theory. These considerations were comprehensively analysed for cohesive-like interfaces in [16,19,31,32]. In this regard, Ortiz and Pandolfi [24] proposed a surface-like finite elements in which the normal and tangential directions to the surface are monitored, and every geometrical operation is carried out on the middle surface of the element. This procedure allows superimposed rigid motions to be overcome. Alternatively, Qiu, et al. [33] applied a simple corotational formulation to one-dimensional interface elements, whereas Reinoso and Paggi developed 2D [19] and 3D [34] interface elements for large deformation analysis dealing with geometrical and material nonlinearities using a consistent derivation of the corresponding operators.

Differing from precedent methodologies for triggering interface cracking that incorporate geometrically nonlinear effects, the authors proposed an alternative formulation [35], that is denominated a “consistent finite displacement and rotation formulation of the Linear Elastic Brittle Interface Model”. This interface model can be easily integrated within standard continuum finite elements as a user-defined material subroutine and accounts for the potential effects of

in-plane or longitudinal normal deformations (variations along the bondline direction). Complying with such modelling technique, the separation between top and bottom surfaces with respect to the interface midplane can be determined through the deformation gradient  $\mathbf{F}$  under large displacement conditions. This standpoint presents some advantages over other methods, such as its simplicity (the coding of a new element formulation is not required) and the computation of a complete displacement field including transverse normal gap  $\delta_n$ , tangential shear gap  $\delta_s^t$  and longitudinal shear or in-plane gap  $\delta_s^l$ , as shown in Fig. 1. Thus, recalling the predictions presented in Ref. [35], the new geometrically nonlinear LEBIM formulation does offer very promising results and notably simplifies the implementation requirements. Within this context, the principal objective of the current investigation is the comprehensive validation of the geometrically nonlinear LEBIM [35] for mixed-mode loading conditions and for its usage in structured interfaces as in Refs. [36,37].

The organization of the manuscript is as follows. Section 2 describes the interface modeling. The validation of the current interface model through its assessment for Double Cantilever Beam (DCB), Mixed Mode Bending (MMB) and End Notch Flexure (ENF) tests is detailed in Section 3, whereas its application to structured interfaces is presented in Section 4. Finally, the main conclusions of this investigation are summarized in Section 5.

## 2. Interface modelling: General aspects and formulation

### 2.1. Geometrically nonlinear interface model

This Section presents the main aspects of the new LEBIM formulation for geometrically nonlinear applications. The current formulation is compatible with general-purpose solid elements and it is subsequently particularized for 2D analysis. Complying with a finite thickness interface model that can be integrated into standard continuum finite elements, the required displacements for the evaluation of the LEBIM traction-separation law, i.e. the relative transverse normal displacement  $\delta_n$ , the tangential shear displacement  $\delta_s^t$  and the longitudinal shear or in-plane displacement  $\delta_s^l$ , are referred to the element midline. Thus, the tracking of this midline can be performed using a material user-subroutine UMAT supported by the commercial software ABAQUS® [38]. See a comprehensive description of the computations at the material point level in Ref. [35].

Assuming the finite displacement theory [39], the deformation gradient  $\mathbf{F}$  is a two-point tensor that relates current  $\mathbf{x}$  and initial  $\mathbf{X}$  configurations, considering deformations as well as rigid body motions. In this modelling framework, two different standpoints can be adopted: Lagrangian or material description, in which the variables are referred to the initial configuration, or Eulerian or spatial description, in which the variables are referred to the current configuration according to

$$\mathbf{F} = \frac{\partial \mathbf{x}}{\partial \mathbf{X}} = \begin{bmatrix} F_{11} & F_{12} \\ F_{21} & F_{22} \end{bmatrix}. \quad (1)$$

The computation of the polar decomposition allows the deformation gradient  $\mathbf{F}$  to be split into the stretch and rotation tensors. As recalled in Ref. [35], this operation can be executed in two ways: (i) the application of the deformation is applied first, and then rotation (material description, Eq. (2)), or conversely (ii) the application of the rotation is followed by the insertion of the deformation at the material point level (spatial description, Eq. (3)), as

$$\mathbf{F} = \mathbf{R}\mathbf{U}, \quad (2)$$

$$\mathbf{F} = \mathbf{V}\mathbf{R}, \quad (3)$$

where  $\mathbf{R}$  is the rotation tensor,  $\mathbf{U}$  is the stretch tensor according to a material description and  $\mathbf{V}$  is the stretch tensor following a spatial

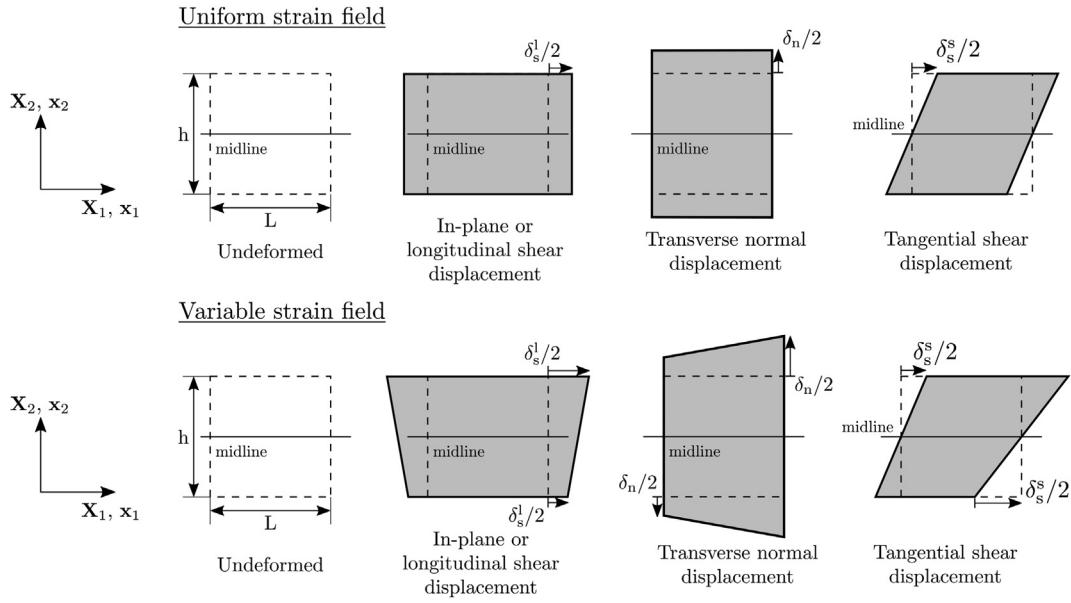


Fig. 1. Displacement field within a 2D element in the interface model under uniform and variable strain field: transverse normal  $\delta_n$ , longitudinal shear or in-plane  $\delta_s^l$  and tangential shear  $\delta_s^s$ .

description. A graphical representation of the motion considering finite strain theory is depicted in Fig. 2.

For the sake of simplicity, the former expression is used within this study, adopting a Lagrangian standpoint. The computation of the element midline rotation can be obtained through the following expression

$$\tan(\alpha_c) = \frac{F_{21}}{F_{11}}, \quad (4)$$

where the significance of the angle  $\alpha_c$  is shown in Fig. 2. Accordingly, the rotation and stretch tensors,  $\mathbf{R}$  and  $\mathbf{U}$ , can be easily calculated as

$$\mathbf{R} = \begin{bmatrix} \cos(\alpha_c) & -\sin(\alpha_c) \\ \sin(\alpha_c) & \cos(\alpha_c) \end{bmatrix}, \quad (5)$$

$$\mathbf{U} = \mathbf{R}^T \mathbf{F} = \begin{bmatrix} U_{11} & U_{12} \\ 0 & U_{22} \end{bmatrix}. \quad (6)$$

Thus, the deformation tensor can be obtained in a straightforward manner by taking into account the rotation of the midline element. Further details about the procedure to obtain  $\alpha_c$ , components of the  $\mathbf{U}$  tensor and differences with respect to regular continuum elements can be found in Ref. [35]. The next ingredient for the evaluation of the TSL is the computation of the displacement jumps across the interface:  $\delta_n$ ,  $\delta_s^s$  and  $\delta_s^l$ . The computation of the displacement vector can be

recalled via the definition of the displacement field variation. This expression shows the relation between the deformation gradient tensor  $\mathbf{F}$  and the undeformed vector  $d\mathbf{X}$  as

$$d\mathbf{x} = d\mathbf{X} + d\mathbf{u} \Rightarrow d\mathbf{u} = d\mathbf{x} - d\mathbf{X} = (\mathbf{F} - \mathbf{I})d\mathbf{X}. \quad (7)$$

In absence of a rigid body rotation, the tensor  $\mathbf{R}$  is equal to the identity matrix and the relative displacements can be expressed as

$$d\mathbf{u} = (\mathbf{U} - \mathbf{I})d\mathbf{X}. \quad (8)$$

From a different perspective, in terms of a generalised material strain tensor of order  $n$ , the corresponding strain tensors can be computed as

$$\mathbf{E}^n = \frac{1}{n}(\mathbf{U}^n - \mathbf{I}), \quad (9)$$

$$\mathbf{E}^1 = (\mathbf{U} - \mathbf{I}). \quad (10)$$

The operator  $(\mathbf{U} - \mathbf{I})$  can be seen as the material strain tensor of order  $n = 1$  (Eq. (10)) or the so-called Biot strain tensor. Restricting our attention to the definition of the first order strain tensor, one obtains

$$\mathbf{E}^1 = \begin{bmatrix} U_{11} - 1 & U_{12} \\ 0 & U_{22} - 1 \end{bmatrix} = \begin{bmatrix} \frac{\partial \delta_s^l}{\partial X_1} & \frac{\partial \delta_s^s}{\partial X_2} \\ 0 & \frac{\partial \delta_n}{\partial X_2} \end{bmatrix}. \quad (11)$$

Through the proper selection of the undeformed element dimensions,  $L$  and  $h$ , as the initial vectors  $dX_1$  and  $dX_2$ , respectively, the displacement jumps can be computed as follows

$$\delta_s^l = (U_{11} - 1)dX_1 = (U_{11} - 1)L, \quad (12)$$

$$\delta_n = (U_{22} - 1)dX_2 = (U_{22} - 1)h, \quad (13)$$

$$\delta_s^s = U_{12}dX_2 = U_{12}h. \quad (14)$$

In applications experiencing rigid body rotations, the motion can be described as follows: firstly, the element is deformed (material description) through the material stretch tensor  $\mathbf{U}$  and the gap displacements or separations  $\delta_n$ ,  $\delta_s^s$  and  $\delta_s^l$  are determined; secondly, the element is rotated via the tensor  $\mathbf{R}$  in order to get the current position.

The extension of this procedure to 3D applications would require the calculation of three angles in order to track the motion of the

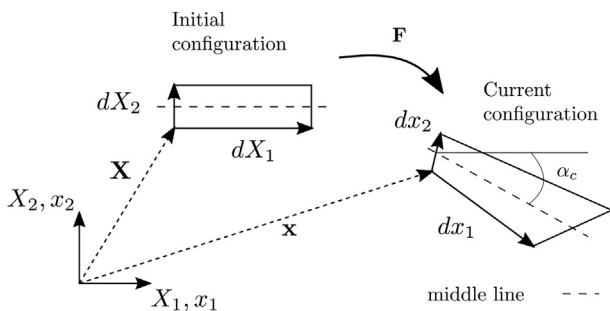


Fig. 2. Initial and current configurations of an element and its relation through the deformation gradient tensor  $\mathbf{F}$ .

element's middle plane during the analysis. That is, the position of the current axis (placed on the element's midplane) with respect to the reference configuration is described by three rotations. This fact increases the complexity of the procedure in comparison to 2D analyses, where only a single angle is needed to characterise the midline behaviour. Nevertheless, the application of analogue procedures to the 2D analysis to the different directions will lead to the rotation matrix and the displacement field in 3D scenarios. Regarding LEBIM, 3D proposals for small displacement scenarios have been recently used for some problems including composite laminates [3,7].

2.2. Constitutive interface equations: Linear Elastic Brittle Interface Model

Once the separation gaps at an interface are computed, the next phase requires the determination of the traction vector for the evaluation of the TSL that characterizes the interface failure. As stated above, in the related literature there are a wide variety of traction-separation laws (bilinear, exponential, trapezoidal, etc) enabling the characterization of different interface behaviours (ductile, brittle, etc). In this investigation the Linear Elastic Brittle Interface Model (LEBIM) is employed, in which the traction and energy standpoints merge in a unique criterion. Nevertheless, it is worth mentioning that the current methodology can be applicable to any different profile of TSL without limitations.

In a general sense, the LEBIM is herewith used to characterize the interface between two solids or a thin adhesive layer, whose stress profile along the thickness is uniform. This technique can be conceived as an elastic spring foundation with a cut-off traction response, that features abrupt failure [3,29]. Accordingly, energy dissipation before crack propagation is considered as negligible and, therefore, no softening area ahead of the crack tip should be appreciated in the problem. Additionally, as was observed in Refs. [3,7], if the stiffness of the system is mostly governed by the adherents, the shape of the TSL has a minor influence on the corresponding overall results, i.e. classical cohesive zone models (with a large softening zone) will lead to similar results as those obtained by LEBIM.

Specifically, tractions  $t$  and energy stored  $G$  in this "spring distribution" are used to compute the mixed mode ratio  $B = G_{II}/G_I$ , where  $G_T = (G_I + G_{II})$ , the critical fracture energy  $G_c$  and the failure instant. Following [29], let tractions be described in terms of displacement jumps across the interface by means of a linear elastic law as

$$t_n = \begin{cases} k_n \delta_n, & \text{if } \delta_n \leq \delta_n^c \\ 0, & \text{otherwise} \end{cases} \quad (15)$$

$$t_s = \begin{cases} k_s \delta_s^c + k_s \delta_s^l = k_s \delta_s, & \text{if } |\delta_s^c| \leq |\delta_s^l| \\ 0, & \text{otherwise} \end{cases} \quad (16)$$

where  $t_n$  and  $t_s$  are normal and shear tractions,  $\delta_n$ ,  $\delta_s^c$  and  $\delta_s^l$  are relative transverse normal, tangential shear and in-plane displacements and  $k_n$  and  $k_s$  are normal and shear stiffnesses, respectively. Note that the shear jump  $\delta_s$  admits two contributions  $\delta_s = \delta_s^c + \delta_s^l$  and that  $k_n$  and  $k_s$  are expressed in  $\frac{\text{MPa}}{\text{mm}}$ . Fig. 3 depicts the behaviour of LEBIM constitutive law.

Notwithstanding, tractions drop to zero when  $t^c$  is reached or, in energy terms, if the energy stored  $G$  fulfills the fracture toughness criterion:  $G = G_c$ . Hence, the definition of the energy release rate stored  $G$  and fracture toughness  $G_c$  is fundamental in the failure description. In this way, the energy contributions can be split into those associated with fracture Mode I and Mode II counterparts ( $G_I$  and  $G_{II}$  respectively) for mixity purposes, which respectively correspond to normal and shear behaviour according to the expressions

$$G = G_I + G_{II}, \quad (17)$$

$$G_I = \frac{\langle t_n \rangle_+ \langle \delta_n \rangle_+}{2} = \frac{\langle t_n \rangle_+^2}{2k_n}, \quad (18)$$

$$G_{II} = \frac{t_s \delta_s}{2} = \frac{t_s^2}{2k_s}, \quad (19)$$

where  $G_I$  and  $G_{II}$  are the energy release rates for fracture Mode I and Mode II, respectively. In the previous expressions, the symbol  $\langle \rangle$  stands for the Macaulay brackets, and therefore only positive values of normal tractions and relative displacements are used for the  $G_I$  calculation.

Finally, a critical fracture energy criterion involving any mixed mode condition  $G_c(B)$  establishes the limit condition. Without any loss of generality, we advocate in the present investigation the use of the phenomenological Benzeggah-Kenane (BK) criterion [40], whose mathematical expression renders

$$G_c = G_{Ic} + (G_{IIc} - G_{Ic}) \left( \frac{G_{II}}{G_I + G_{II}} \right)^\eta, \quad (20)$$

where  $\eta$  is a material coefficient as described in Ref. [41].

2.3. Snap-back control algorithm

From a numerical point of view, in simulations involving damage progression, nonlinear effects play an important role in achieving equilibrium solutions, i.e. dictating convergence. Usually, in the majority of tests or applications, the boundary conditions are conceived with the aim of either reproducing the experimental gripping conditions in the tests or reflecting the loading conditions of theoretical analysis. These external solicitations are generally imposed by monotonically increasing/decreasing loads/displacements in specific positions of the specimen with the purpose of obtaining a particular stress, strain

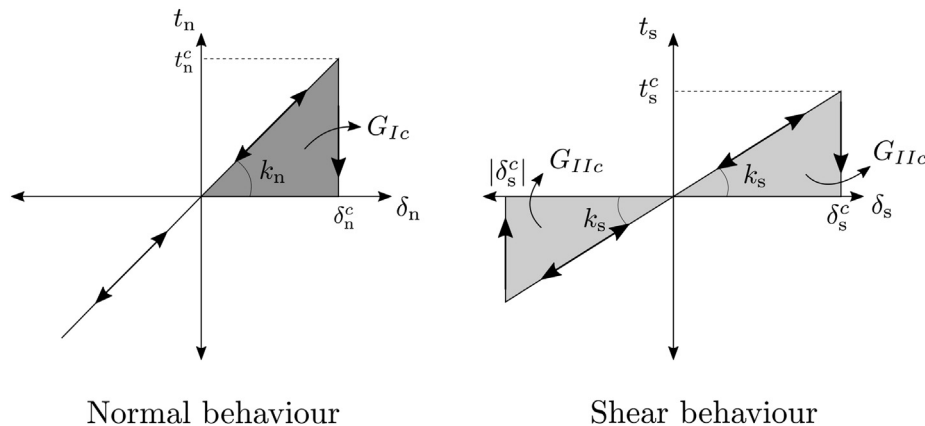


Fig. 3. Linear Elastic Brittle Interface Model: traction-separation law in normal ( $t_n - \delta_n$ ) and shear ( $t_s - \delta_s$ ) directions.

or displacement field. However, due to the onset of failure processes and fracture propagation, the linearity of the solution is compromised and the redistribution of the stress field may lead to simultaneous reduction in load and displacement, snap-back behaviours. These snap-backs jeopardize the convergence of the simulation employing load or displacement controlled boundary conditions. Although there are methods that consider changes in the direction of the load–displacement curves, for instance the Riks method [42], other techniques have been developed in order to overcome these instabilities in an efficient manner.

In this setting, Tvergaard [43] proposed an alternative to capture fluctuations in the load–displacement curves by finding a variable that increases monotonically during the simulation. In this way, the control is applied in such variable and the loads and displacements at the boundary are computed as output variables of the finite element analysis. This approach allows the Newton–Raphson algorithm to be used without any further modifications, and has been tested in simulations including sphere fracture in composites made up of random distribution of elastic spheres within an elasto-plastic matrix [44], or the investigation of gradient-enhanced dislocation hardening on the mechanics of notch-induced failure [45]. Mainly, the control is applied: (i) to the sum of the opening displacements of some nodes ahead of the crack tip, in presence of a unique interface, or (ii) the relative opening within the interfaces along the loading direction, if more than one interface is involved. In this study, we are focused on the former approach, which is concisely described in the following paragraphs with focus on MMB specimens.

To commence the description of this control algorithm, let  $N_1$  and  $N_2$  be the nodes belonging to upper and bottom surfaces of the interface, respectively, and  $N_C$  a dummy node that can be placed at any point, as depicted in Fig. 4. Likewise,  $N_C$  will be the control node and  $N_L$  the node in which the load or displacement conditions at the boundary are applied. The relative displacement at the interface, corresponding to the global basis  $\{X_1, X_2\}$ , can be related to the control node  $N_C$  by making use of the AUXILIARY ELEMENTS of a FEM code (ABAQUS being used in the present investigation) as follows

$$\begin{bmatrix} 0 & 0 & 0 \\ 0 & 0 & 0 \\ 1 & -1 & 0 \end{bmatrix} \begin{bmatrix} u_{X_1}^{N_1} \\ u_{X_1}^{N_2} \\ u_{X_1}^{N_C} \end{bmatrix} = \begin{bmatrix} f_{X_1}^{N_1} \\ f_{X_1}^{N_2} \\ f_{X_1}^{N_C} \end{bmatrix}, \quad (21)$$

$$\begin{bmatrix} 0 & 0 & 0 \\ 0 & 0 & 0 \\ 1 & -1 & 0 \end{bmatrix} \begin{bmatrix} u_{X_2}^{N_1} \\ u_{X_2}^{N_2} \\ u_{X_2}^{N_C} \end{bmatrix} = \begin{bmatrix} f_{X_2}^{N_1} \\ f_{X_2}^{N_2} \\ f_{X_2}^{N_C} \end{bmatrix}, \quad (22)$$

where  $u_{X_1}$  and  $u_{X_2}$  are nodal displacement in global directions and  $f_{X_1}$  and  $f_{X_2}$  are the corresponding nodal forces. In the FE analysis the relative displacement at the interface,  $(u_{X_1}^{N_1} - u_{X_1}^{N_2})$  or  $(u_{X_2}^{N_1} - u_{X_2}^{N_2})$ , is set by prescribing the nodal force of the control node  $f_{X_1}^{N_C}$  or  $f_{X_2}^{N_C}$ . Next, Eq. (21) is employed to prescribed the opening displacement along the  $X_1$  global direction, whereas Eq. (22) is used to set nodal relative displacements along the  $X_2$  global direction. A flowchart of the current procedure is given in Fig. 4 for the sake of clarity. A general implementation in a FE package would require the description and adaptation of the method based on the particular characteristics of the FE-code. In any case, a more detailed description can be found in Ref. [46].

Finally, the nodal force at the boundary  $f_{X_1}^{N_L}$  or  $f_{X_2}^{N_L}$  is equal to the displacement of the control node  $u_{X_1}^{N_C}$  or  $u_{X_2}^{N_C}$ . This relation can be defined through the definition of a new AUXILIARY ELEMENT following

$$\begin{bmatrix} 0 & 1 \\ 0 & 0 \end{bmatrix} \begin{bmatrix} u_{X_2}^{N_L} \\ u_{X_2}^{N_C} \end{bmatrix} = \begin{bmatrix} f_{X_2}^{N_L} \\ f_{X_2}^{N_C} \end{bmatrix}, \quad (23)$$

$$\begin{bmatrix} 0 & 0 & 0 & 0 \\ 0 & 0 & 1 & 0 \\ 0 & 0 & 0 & 0 \\ 0 & 0 & 0 & 0 \end{bmatrix} \begin{bmatrix} u_{X_1}^{N_L} \\ u_{X_2}^{N_L} \\ u_{X_1}^{N_C} \\ u_{X_2}^{N_C} \end{bmatrix} = \begin{bmatrix} f_{X_1}^{N_L} \\ f_{X_2}^{N_L} \\ f_{X_1}^{N_C} \\ f_{X_2}^{N_C} \end{bmatrix}, \quad (24)$$

where Eq. (23) relates the reaction of the normal opening displacement at the interface  $u_{X_2}^{N_C}$  to the nodal force in  $X_2$  direction  $f_{X_2}^{N_L}$  and Eq. (24) associates the reaction of the shear displacement at the interface  $u_{X_1}^{N_C}$  to the nodal force in  $X_2$  direction  $f_{X_2}^{N_L}$ .

It should be mentioned that previous operators usually represent a stiffness matrix that relates nodal displacements to nodal forces, so that the components of such matrix should have [Force/displacement] dimensions. Differing from this, the capabilities of the AUXILIARY ELEMENTS are employed in the present analysis in a different way:

- The AUXILIARY ELEMENTS, presented in Eqs. (21) and (22), relate the relative nodal displacement at the interface to the displacements of the control node, so that the components of the matrix associated with this AUXILIARY ELEMENT are dimensionless. Nevertheless, the conventional finite element nomenclature remains for the sake of the consistency. That is, the variable  $f^{N_C}$  is calculated as a force unknown in the global system of the Finite Element model, but this variable actually stands for the nodal displacement of the node  $N_C$ . On the contrary,  $u^{N_C}$  represents the reaction force of such node.
- The AUXILIARY ELEMENTS, displayed in Eqs. (23) and (24), relate the nodal force of the control node  $N_C$  to the nodal forces at the boundary, specifically to the node  $N_L$  in the current case. Hence, the components of the matrix associated with these AUXILIARY ELEMENTS are dimensionless. In this way, the reaction force of the control node, named as  $u^{N_C}$ , is related to the nodal force at the boundary, represented by the variable  $f^{N_L}$ . The specific components of the AUXILIARY ELEMENT will determine the relationship between the degrees of freedom and the direction of the nodal forces corresponding to  $N_C$  and  $N_L$  nodes.

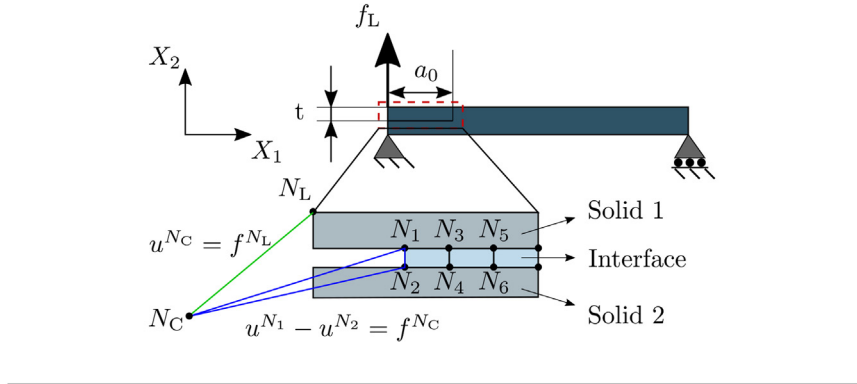
Note however that in situations where more than one pair of nodes are implied in the process, that is, the AUXILIARY ELEMENTS (Eqs. (21) and (22)) are applied to additional pairs of nodes, the nodal force of the control node  $f^{N_C}$  represents the sum of the opening displacement of each paired nodes. This scheme may be useful to track the global tendency at the interface instead of focusing in a particular pair of nodes.

These equations are added to the global stiffness matrix of the system in order to compute the unknown variables, in this case the displacement in the control node  $u^{N_C}$  and the displacement of the boundary node  $u^{N_L}$ . It is worth to emphasize that  $u^{N_C}$ , through the AUXILIARY ELEMENT materialised in the Eqs. (21) and (22), corresponds to the reaction force of the boundary node:  $u^{N_C} = f^{N_L}$ . Therefore, both displacement and force at the boundary,  $u^{N_L}$  and  $f^{N_L}$ , respectively, are calculated as any degree of freedom of the system and they may present non-monotonic behaviour.

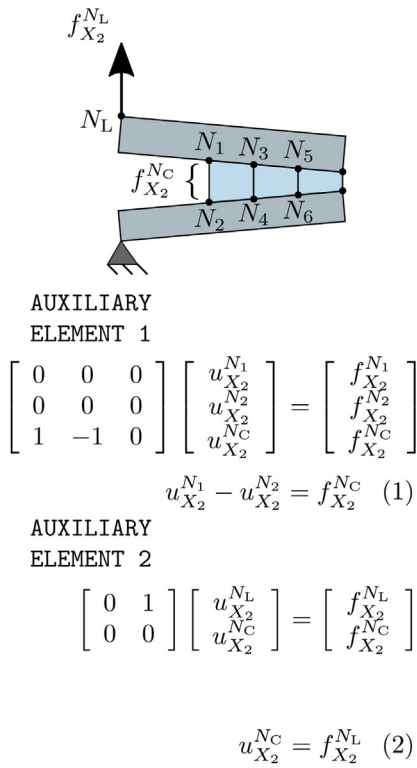
As a summary, the control algorithm is outlined in the following scheme:

1. Define a control node  $N_C$  anywhere.
2. Prescribe the opening displacement along the interface by means of the control node  $f^{N_C}$  and the AUXILIARY ELEMENT 1.  
 $u^{N_1} - u^{N_2} = f^{N_C}$
3. Relate the displacement of the control node to the nodal force at the boundary through the AUXILIARY ELEMENT 2.  
 $u^{N_C} = f^{N_L}$
4. Include these equations or constraints to the global stiffness matrix.
5. Obtain  $u^{N_L}$  and  $f^{N_L}$  as part of the system solution.

**General framework**



**Normal displacement**



**Shear displacement**

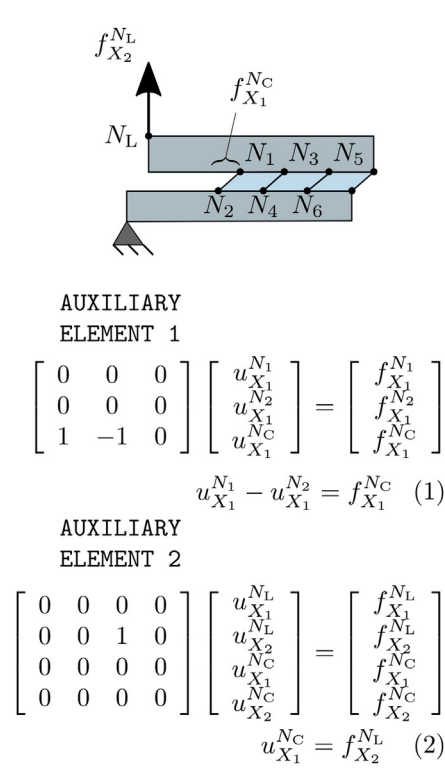


Fig. 4. Scheme of the control algorithm:  $N_1$ – $N_6$  are interface nodes,  $N_C$  is the control node and  $N_L$  is the node where the boundary conditions are established.  $u$  and  $f$  stand for nodal displacements and nodal forces at the corresponding nodes.

**3. Application of the geometrically nonlinear LEBIM to general mixed mode fracture tests: DCB, MMB and ENF**

This Section outlines the validation of the proposed geometrically nonlinear LEBIM for its application to general mixed-mode fracture tests. In particular, we specialize this procedure to numerical-experimental correlation of well established tests: (i) DCB test for fracture Mode I conditions, (ii) MMB test for mixed-mode fracture conditions and (iii) ENF test for fracture Mode II characterization. With the purpose of testing the accuracy of the interface approach presented above, predictions of such tests, involving delamination events under different loading conditions, are compared with the experimental data extracted from Ref. [47]. Note also that other authors [1,2] have previously assessed their corresponding interface decohesion elements with respect to these experiments. It is worth mentioning that, in the

following simulations, the in-plane stiffness of the current LEBIM is set equal to zero, neglecting the in-plane deformation effects, with the aim of comparing the performance of the present formulation with respect to alternative cohesive elements [1,2,16].

Simulations are carried out using specimens with the following geometrical dimensions: 50 mm in length of half-span  $L_{beam}$ , 25 mm in width and 1.55 mm half-thickness  $t$ . This set up is defined according to the test configuration specified in Fig. 5, and it is usually denominated as the MMB method, which allows assessing different mixed-mode fracture ratios using the same specimen configuration. This can be achieved via the definition of a parametric length  $c$ , whose value can be set accordingly to range from pure fracture Mode I to pure fracture Mode II, covering a wide range of mode-mixity ratios. Based on this configuration and recalling standard Bernoulli beam theory, the ratio between the middle and end forces, denoted by  $P_M$  and  $P_E$ ,

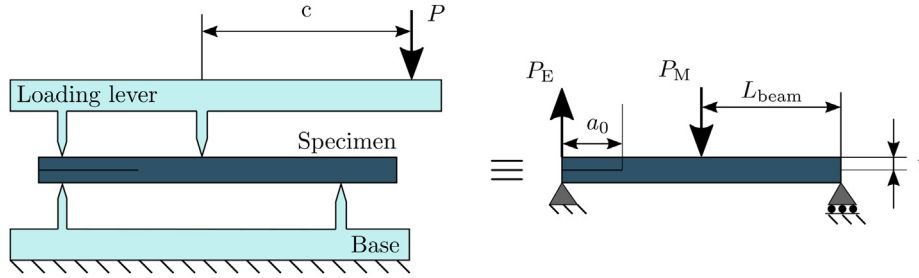


Fig. 5. Mixed Mode Bending test: boundary conditions and specimen dimension.  $P_E$  and  $P_M$  represent the loads applied at the left end and the middle of the specimen.  $L_{\text{beam}}$  and  $t$  stand for the semi-length and one-arm thick of the coupon, whereas  $a_0$  indicates the length of the initial delamination.

Table 1

Initial crack length  $a_0$ , length of the lever  $c$  and middle-end load ratio  $P_M/P_E$ , according to Fig. 5, for different mixed-mode ratios  $G_{II}/G_T$ .

$G_{II}/G_T$	0.0 (DCB)	0.2	0.5	0.8	1.0 (ENF)
$a_0$ [mm]	32.9	33.7	34.1	31.4	39.3
$c$ [mm]	—	97.4	42.2	27.6	—
$P_M/P_E$ [-]	0.0	1.46	2.14	2.79	$\infty$

respectively, can be related to specific mixed-mode ratios  $G_{II}/G_T$  (see [2] for further details).

Additionally to the previous characteristics, an initial crack length  $a_0$  is defined between 30 mm and 40 mm in order to achieve a stable crack propagation, Fig. 5. The corresponding pre-crack lengths  $a_0$ , the length of the lever  $c$  and the relation between the end and the middle load  $P_M/P_E$  for each of the configurations analysed herein are detailed in Table 1, emphasizing the mixed-mode fracture ratios. The material properties of the laminates (AS4/PEEK composite) are reported in Table 2. The specimens are composed of 24 unidirectional plies, employing a Kapton film to induce the initial crack length.

Regarding the characteristics of the numerical models, the adherents are simulated complying with a linear elastic composite material law, whereas the proposed LEBIM is employed to describe the interface behaviour between the two arms. The baseline numerical model is generated using approximately 5800 2D plane strain elements for the discretization of the entire model, where about 300 of those elements correspond to interface elements that were equipped with LEBIM. The undeformed mesh size at the region of interest is around 0.25 mm in width and 0.05 mm in height. Table 3 shows the input properties for the interface elements [2].

The control algorithm described in Section 2.3 is also applied in the current simulations in order to preclude numerical difficulties for the achievement of converged equilibrium solutions. Such procedure is correspondingly adapted to each configuration (DCB, MMB and ENF) according to the mode mixity of the tests and the relative displacement at the crack tip. Additionally, a new AUXILIARY ELEMENT is defined in order to establish the relationship between the forces at the end and at the middle of the specimen,  $f_{X_2}^{N_E}$  and  $f_{X_2}^{N_M}$  respectively (Section 2.3). Note the distinction between beam-theory values  $P_M$  and  $P_E$  and the finite element values  $f_{X_2}^{N_E}$  and  $f_{X_2}^{N_M}$  to denote the nodal boundary forces. In this way, the relation  $P_M/P_E$  is constant during the test according to the length of the lever  $c$  [2], as shown in Table 1, and such relation is

Table 2

AS4/PEEK properties.

$E_{11}$	$E_{22} = E_{33}$	$G_{12} = G_{13}$	$G_{23}$	$\nu_{12} = \nu_{13}$	$\nu_{23}$
129 GPa	10.1 GPa	5.5 GPa	3.7 GPa	0.25	0.45

imposed in the FE simulation. Fig. 6 comprehensively details the procedure to apply normal or shear separations at the crack tip, and the way through which the link between the nodal forces at the boundary ( $f_{X_2}^{N_E}$  and  $f_{X_2}^{N_M}$ ) and the control node is constructed in order to obtain the desired relation.

The normal displacement depicted in Fig. 6 is applied in the DCB and MMB tests. In this regard, with respect to the MMB simulations, we set the ratios  $G_{II}/G_T = 0.2$  and  $G_{II}/G_T = 0.5$  using this normal displacement. Moreover, in additional computations, the shear displacement approach in Fig. 6 is employed for the simulation of MMB configurations with  $G_{II}/G_T = 0.8$  and for the ENF test.

Fig. 7 shows the correlation between experimental and numerical results concerning load–displacement curves. In this graph, noticeable snap-back effects throughout the crack propagation in numerical simulations can be identified. This is associated with the boundary conditions imposed in the analysis, in this case an increasing separation (normal or shear) between the crack flanks. Note also that despite the fact that current boundary conditions do not exactly replicate the experimental gripping conditions, numerical predictions are in very close agreement with respect to the tests data, in both the linear elastic and crack progression regions of the evolutions.

Moreover, the evaluation of the mixed mode ratio  $G_{II}/G_T$  can be performed in a straightforward manner using LEBIM, since only the tractions at the crack tip are required as

$$G_{II}/G_T = \frac{t_s^2/(2k_s)}{(t_n)_+^2/(2k_n) + t_s^2/(2k_s)} = \frac{1}{\left(\frac{(t_n)_+}{t_s}\right)^2 \frac{k_s}{k_n} + 1}. \quad (25)$$

Fig. 8 depicts the evolution of the mixed mode  $G_{II}/G_T$  for each configuration according to the expression given in Eq. (25) as a function of the crack length. Such curves present a constant value during the crack growth in conjunction with some fluctuations lower than the 10% with respect to their mean values. Table 4 reports the qualitative comparison between the experimental and numerical results, where the maximum force  $F_{\text{max}}$  and the mixed mode ratio  $G_{II}/G_T$  are detailed. In the numerical column, the mean value of the curves in Fig. 8 is provided.

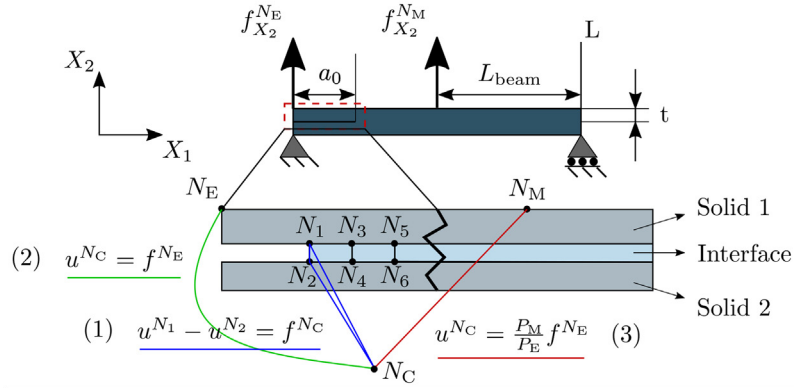
Based on the current results, it is possible to state that the current formulation combining continuum elements and Traction Separation Laws relying on the LEBIM enables capturing the initiation and evolution of delamination events under Mode I, Mode II and mixed mode fracture conditions. Furthermore, from a computational perspective, as shown in Fig. 7, the control algorithm captures the characteristic snap-back curves during crack propagation. Snap-back instabilities are a mathematical artifact resulting from assuming quasi static

Table 3

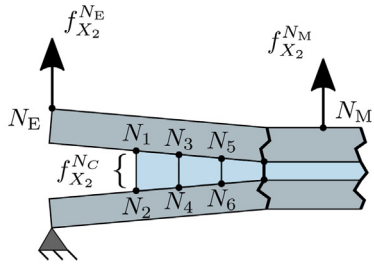
Linear Elastic Brittle Interface Model properties [2].

$t_n^c$ [MPa]	$t_s^c$ [MPa]	$G_{Ic}$ [kJ/m <sup>2</sup> ]	$G_{IIc}$ [kJ/m <sup>2</sup> ]	$\eta$ [-]
80	100	0.969	1.719	2.284

**General framework**



**Normal displacement**



AUXILIARY ELEMENT 1

$$\begin{bmatrix} 0 & 0 & 0 \\ 0 & 0 & 0 \\ 1 & -1 & 0 \end{bmatrix} \begin{bmatrix} u_{X_2}^{N_1} \\ u_{X_2}^{N_2} \\ u_{X_2}^{N_C} \end{bmatrix} = \begin{bmatrix} f_{X_2}^{N_1} \\ f_{X_2}^{N_2} \\ f_{X_2}^{N_C} \end{bmatrix}$$

$$u_{X_2}^{N_1} - u_{X_2}^{N_2} = f_{X_2}^{N_C} \quad (1)$$

AUXILIARY ELEMENT 2

$$\begin{bmatrix} 0 & 1 \\ 0 & 0 \end{bmatrix} \begin{bmatrix} u_{X_2}^{N_E} \\ u_{X_2}^{N_C} \end{bmatrix} = \begin{bmatrix} f_{X_2}^{N_E} \\ f_{X_2}^{N_C} \end{bmatrix}$$

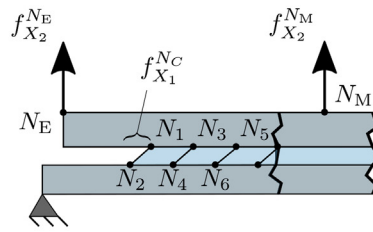
$$u_{X_2}^{N_C} = f_{X_2}^{N_E} \quad (2)$$

AUXILIARY ELEMENT 3

$$\begin{bmatrix} 0 & -\frac{P_M}{P_E} \\ 0 & 0 \end{bmatrix} \begin{bmatrix} u_{X_2}^{N_C} \\ u_{X_2}^{N_M} \end{bmatrix} = \begin{bmatrix} f_{X_2}^{N_M} \\ f_{X_2}^{N_C} \end{bmatrix}$$

$$-\frac{P_M}{P_E} u_{X_2}^{N_C} = f_{X_2}^{N_M} \quad (3)$$

**Shear displacement**



AUXILIARY ELEMENT 1

$$\begin{bmatrix} 0 & 0 & 0 \\ 0 & 0 & 0 \\ 1 & -1 & 0 \end{bmatrix} \begin{bmatrix} u_{X_1}^{N_1} \\ u_{X_1}^{N_2} \\ u_{X_1}^{N_C} \end{bmatrix} = \begin{bmatrix} f_{X_1}^{N_1} \\ f_{X_1}^{N_2} \\ f_{X_1}^{N_C} \end{bmatrix}$$

$$u_{X_1}^{N_1} - u_{X_1}^{N_2} = f_{X_1}^{N_C} \quad (1)$$

AUXILIARY ELEMENT 2

$$\begin{bmatrix} 0 & 0 & 0 & 0 \\ 0 & 0 & 1 & 0 \\ 0 & 0 & 0 & 0 \\ 0 & 0 & 0 & 0 \end{bmatrix} \begin{bmatrix} u_{X_1}^{N_L} \\ u_{X_2}^{N_L} \\ u_{X_1}^{N_C} \\ u_{X_2}^{N_C} \end{bmatrix} = \begin{bmatrix} f_{X_1}^{N_L} \\ f_{X_2}^{N_L} \\ f_{X_1}^{N_C} \\ f_{X_2}^{N_C} \end{bmatrix}$$

$$u_{X_1}^{N_C} = f_{X_1}^{N_E} \quad (2)$$

AUXILIARY ELEMENT 3

$$\begin{bmatrix} 0 & 0 & 0 & 0 \\ 0 & 0 & -\frac{P_M}{P_E} & 0 \\ 0 & 0 & 0 & 0 \\ 0 & 0 & 0 & 0 \end{bmatrix} \begin{bmatrix} u_{X_1}^{N_M} \\ u_{X_2}^{N_M} \\ u_{X_1}^{N_C} \\ u_{X_2}^{N_C} \end{bmatrix} = \begin{bmatrix} f_{X_1}^{N_M} \\ f_{X_2}^{N_M} \\ f_{X_1}^{N_C} \\ f_{X_2}^{N_C} \end{bmatrix}$$

$$-\frac{P_M}{P_E} u_{X_1}^{N_C} = f_{X_2}^{N_M} \quad (3)$$

**Fig. 6.** Scheme of the control algorithm for Mixed Mode Bending test:  $N_1-N_6$  are interface nodes,  $N_C$  is the control node and  $N_L$  is the node where the boundary conditions are established.  $u$  and  $f$  stand for nodal displacements and nodal forces in the corresponding nodes.  $N_E$  and  $N_M$  correspond to the nodes located at the left end and at the middle, respectively, at the top surface of the upper adherent.

conditions and are therefore not present in experiments, where unstable crack growth is a local dynamic effect. Regarding the mixity of the MMB tests, the mixed mode value derived from LEBIM formulation (Eq. (25)) slightly differs from the predicted value of  $G_{II}/G_T$  using

the classical Bernoulli beam theory. This small deviation could be attributed to the fact that the current form of such classical theory does not account for geometrically nonlinear effects that are especially relevant for the MMB configurations.

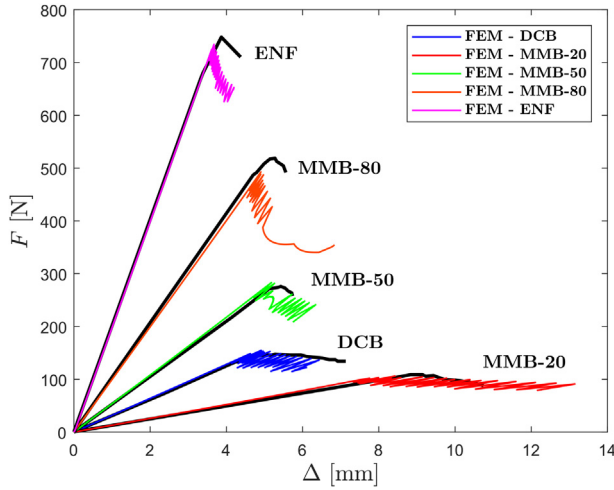


Fig. 7. Correlation between experimental [47] and simulated tests corresponding to DCB, MMB and ENF experiments, including mixed mode ratios  $G_{II}/G_T = [0.00.20.50.81.0]$ .

#### 4. Application of the geometrically nonlinear LEBIM for DCB specimens with hierarchical trapezoidal interfaces

##### 4.1. LEBIM validation by means of experimental–numerical correlation of structured interfaces in DCB tests

This Section addresses the applicability of the proposed geometrically nonlinear LEBIM for the analysis of novel interface profile using structured patterns. This is within the scope of the research activities previously carried out by the authors in Refs. [36,37] in which additive layer manufacturing (ALM) capabilities for composite materials have been exploited.

In particular, we specialize the manufacturing of trapezoidal interface DCB specimens using Glass Fiber Composite (GFC) and nylon. For validation purposes, the flat specimen and one of the patterned configurations experimentally tested in Ref. [37] were analysed using the interface framework in Section 2. The overall dimensions of the coupons employed in the FE simulations are:

- Flat interface:  $h_{GFC} = 2.5$  mm,  $h_{nylon} = 1.5$  mm,  $h_{int} = 0.05$  mm,  $L_{str} = 169$  mm, according to the scheme of Fig. 9.

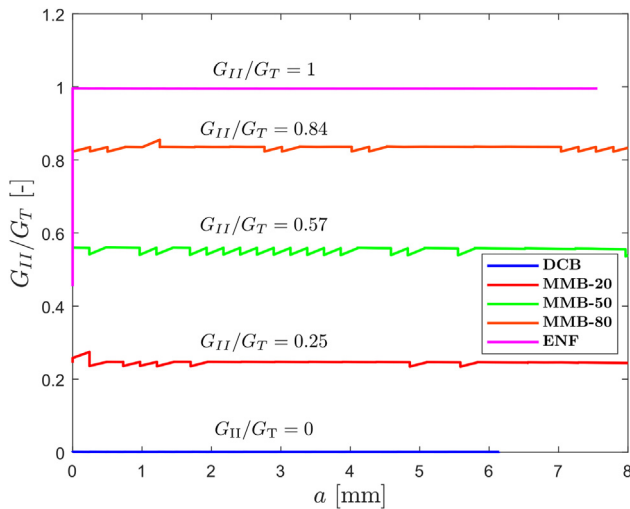


Fig. 8. Mixed mode evolution  $G_{II}/G_T$  at the crack tip (Eq. (25)) corresponding to computational models of DCB, MMB and ENF, including beam-theory mixed mode ratios  $G_{II}/G_T = [0.00.20.50.81.0]$  [2].

Table 4

Experimental [47] versus numerical results.  $F_{max}$  is the maximum load in the test, experimental  $G_{II}/G_T$  is that reported in Ref. [47] (based on beam theory) and Eq. (25) at the crack tip is employed in numerical  $G_{II}/G_T$ .

Experimental		Numerical	
$G_{II}/G_T$	$F_{max}$ [N]	$G_{II}/G_T$	$F_{max}$ [N]
0.00	147.5	0.00	154.6
0.20	108.7	0.25	106.0
0.50	275.8	0.57	283.1
0.80	518.7	0.84	492.8
1.00	748.0	1.00	734.0

- Trapezoidal interface:  $h_{GFC} = 2.5$  mm,  $h_{nylon} = 0.5$ ,  $h_{int} = 0.05$  mm,  $L_{str} = 169$  mm,  $A = 1.7$  and  $\lambda = 8$  mm, according to the scheme of Fig. 9.

As the previous case analysed in Section 3, adherents are simulated using a linear elastic behaviour, no damage emerging then in this part of the specimen, and the adhesive layer is represented by a linear elastic brittle law. Current LEBIM properties along the interface are listed in Table 5 and the GFC and nylon properties are specified in Table 6. In the LEBIM, the stiffness relationship is set to  $k_s/k_n = 1$ . The methodology presented in Section 2.1 was employed to model the interface in the DCB simulations so as to examine the role of the in-plane deformations within the adhesive/interface.

Regarding the FE model, 4-node plane-strain elements (type CPE4 in ABAQUS® library) are employed in the adherents as well as in the interface. In the flat case, around 22k elements constitute the adherents and 576 elements (0.25 mm in length) form the interface region. Conversely, around 140k elements made up the adherents and around 150 elements (0.06 mm in length) form each trapezium.

Two different methods were used to evaluate the fracture energy in the patterned interfaces:

- First, the critical energy release rate  $G_c$ , based on the standards outlined in Ref. [48] and employed previously in Ref. [37], is determined as the area under the load–displacement curve with respect to the effective or apparent cracked surface (crack length  $a_x$  in a 2D analysis) between two different crack lengths, as depicted in Figs. 12 and 17.  $a_{x1}$  and  $a_{x2}$  included in the same plot were employed in the fracture characterisation according to the expression

$$G_c^{LD} = \frac{A^{LD}}{a_{x2} - a_{x1}}. \quad (26)$$

- Second, the effective J-Integral developed in Ref. [36], defined as the variation of the potential energy with respect to the horizontal projection of the crack advance ( $X_1$  global axis)

$$J^X = -\frac{d\Pi}{da_x} = -\int_{\partial\Gamma} \left( \frac{\omega(X_1, X_2)}{\cos(\alpha)} dX_2 - \frac{t_i}{\cos(\alpha)} \frac{\partial u_i}{\partial X_1} ds \right). \quad (27)$$

Decomposing the last expression into symmetrical and anti-symmetrical counterparts, the fracture energy developed in Mode I and Mode II can be obtained by means of the tractions and displacements within the interface as

$$J_I^X = \sum_{k=1}^n J_{I,\Gamma_k+\Gamma_{k'}}(a_x) = \sum_{k=1}^n \int_{\Gamma_k} \frac{t_n}{\cos \alpha} \frac{\partial \delta_n}{\partial X_1} dX_1, \quad (28)$$

$$J_{II}^X = \sum_{k=1}^n J_{II,\Gamma_k+\Gamma_{k'}}(a_x) = \sum_{k=1}^n \int_{\Gamma_k} \frac{t_s}{\cos \alpha} \frac{\partial \delta_s}{\partial X_1} dX_1, \quad (29)$$

where  $\alpha$  is the angle respect to the horizontal plane (see Fig. 9), which depends on the position along the crack path:  $\alpha = \alpha(X_1)$ .  $\Gamma_k$  represents the different sections along the profile. The path selected to perform the J-Integral calculations involved the upper and lower

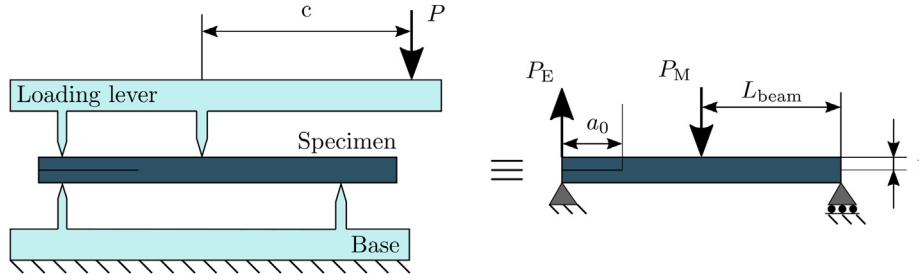


Fig. 9. Double Cantilever Beam specimen with flat and trapezoidal interface. Materials: glass-fibre composite (GFC), nylon and adhesive. Dimensions: length  $L_{scr}$ , height of glass-fibre composite  $h_{GFC}$ , height of nylon in the bulk part  $h_{nylon}$ , amplitude  $A$  and wavelength  $\lambda$  of the trapezoidal interface.

Table 5

Properties of the adhesive modelled as a LEBIM in the experimental–numerical correlation.

Material	$t_n^c$ [MPa]	$t_s^c$ [MPa]	$G_{Ic}$ [J/m <sup>2</sup> ]	$G_{IIc}$ [J/m <sup>2</sup> ]
Adhesive	4.0	16.0	136.3	2180

surfaces of the interface, from the crack tip to the point where the normal stress becomes null. Figs. 13 and 18 shows the evolution of the  $J^X = J_I^X + J_{II}^X$  respect to the effective crack length  $a_x$ . Additionally, for comparing purposes, a mean value of the J-Integral is provided by means of

$$\bar{J}_c^X = \frac{1}{a_{x2} - a_{x1}} \int_{a_{x1}}^{a_{x2}} J^X da_x. \quad (30)$$

This last expression allows a direct comparison with  $G_c$  to be performed due to the fact that for elastic materials  $J = G$ .

Nonetheless, in order to properly exploit the large-displacement procedure pinpointed in Section 2.1 for non-flat interfaces, a pre-process for the interface zone and a slight modification of the UMAT are required. Specifically, an initial rotation of the deformation matrix  $\mathbf{F}$  is performed to obtain the strain field expressed in a coordinate system in accordance with the initial midplane of the interface. It is worth emphasising that in the presence of structured interfaces, the direction of the path  $\alpha_i$  with respect to the global coordinate system  $(X_1, X_2)$  is a function of the position. In this way, Eq. (32) points out the operator that is required in order to get the appropriate reference system as

$$\mathbf{F}_i = \mathbf{R}_i^T \mathbf{F} \mathbf{R}_i, \quad (31)$$

where

$$\mathbf{R}_i = \begin{bmatrix} \cos(\alpha_i) & -\sin(\alpha_i) \\ \sin(\alpha_i) & \cos(\alpha_i) \end{bmatrix}. \quad (32)$$

This operation should be performed at each integration point with its corresponding  $\alpha_i$  value. A PYTHON script was developed to obtain the initial slope for each integration point and it was transferred to the UMAT as a dummy initial state variable by means of the SDVINI user subroutine.

Finally, as the variables of the interface elements were expressed in global coordinates, an additional rotation of the stress tensor and Jacobian matrix is performed. It is worth mentioning that the output vari-

ables of the UMAT should be expressed in the global Cartesian basis. Hence, a rotation of  $-(\alpha + \alpha_i)$  radians is carried out for achieving equilibrium and getting convergence. Fig. 10 shows the pseudo-code used to calculate the tractions and the Jacobian matrix in curved profiles.

The previous algorithm allows for the displacement field along the interface to be computed and, consequently, for comparison between normal, shear and in-plane displacements. Fig. 11 displays a drawing of the deformed DCB specimen and the displacement components  $(\delta_n, \delta_s^s, \delta_s^l)$  along the interface length in an intermediate increment of the simulation. It can be observed that  $\delta_n$  represents the highest values in the displacement field, followed by the shear displacement  $\delta_s^s$ . The in-plane deformations can be considered negligible with respect to  $\delta_n$  or  $\delta_s^s$ . In fact, the in-plane displacements  $\delta_s^l$  do not exceed  $1 \times 10^{-3}$  mm during the test, that is, the maximum in-plane displacement represent the 0.5% of the maximum relative shear displacement and the 0.07% of the maximum relative normal displacement. Hence, neglecting the in-plane deformation in this scenario is an adequate hypothesis (that can be incorporated by setting  $k_i = 0$ ).

Fig. 12 shows the experimental–numerical correlation of the load displacement curves corresponding to the DCB tests in the flat and trapezoidal interfaces. Fig. 13 displays the mixed mode  $J_{II}^X/J_I^X$ , where  $J_T^X = J_I^X + J_{II}^X$ , and the  $J^X$  evolution with respect to the effective crack length  $a_x$  obtained from the FE models.

A good agreement between the curves can be observed in both flat and patterned interfaces. The initial linear-elastic behaviour is captured appropriately as well as the propagation phase, including the unstable crack advance in the trapezoidal case. Furthermore, the prediction of the crack length is in accordance with the experiments. Notwithstanding, the larger discrepancies involving crack length and load–displacement curve occur at the fracture initiation stage. Regarding the mixity of the FE models, the flat configuration led to  $B = 0$ , as expected, whereas the trapezoidal case presents sharp fluctuations along the virtual test whose maximum values are established around  $B = 0.2$ . The J-Integral evolution shares the features of the mixed mode distribution and the average effective energy release rate  $\bar{J}_c^X$  is almost twice higher in the patterned scenario than in the flat interface ( $\bar{J}_c^X = 243.3$  kJ/m<sup>2</sup> in the trapezoidal interface and  $\bar{J}_c^X = 130.3$  kJ/m<sup>2</sup> in the reference scenario). A summary of the results in the experimental and numerical analysis are included in Table 7.

In view of the results, it is remarkable that the energy release rate obtained from the area of the load–displacement curve  $G_c^{LD}$  in the flat case is higher than the experimental one:  $G_{Ic} = 136.3$  kJ/m<sup>2</sup>. This discrepancy may emerge from the difference between experimental and

Table 6

Properties of the glass-fibre composite (GFC) and nylon.

Material	$E_{11}$ [MPa]	$E_{22}$ [MPa]	$E_{33}$ [MPa]	$\nu_{12}$ [–]	$\nu_{13}$ [–]	$\nu_{23}$ [–]	$G_{12}$ [MPa]
GFC	25863	1221	1221	0.45	0.45	0.45	778
Nylon	384	384	384	0.39	0.39	0.39	–

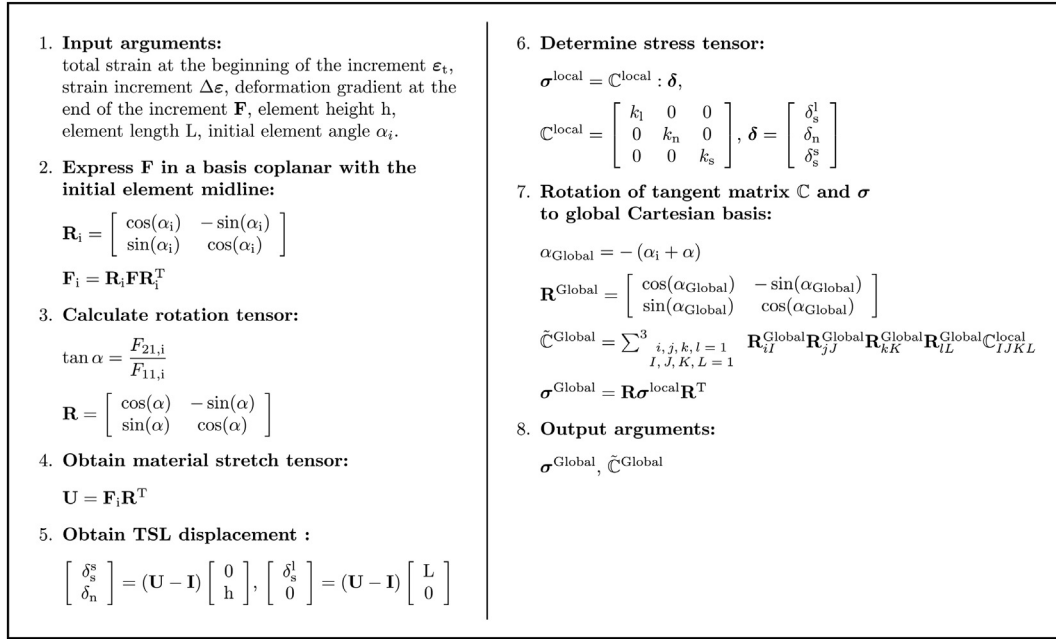


Fig. 10. Simplified algorithm for displacement-stress estimation in a Traction Separation Law presenting a curved crack path in interface continuum elements under finite displacement and rotation assumptions.

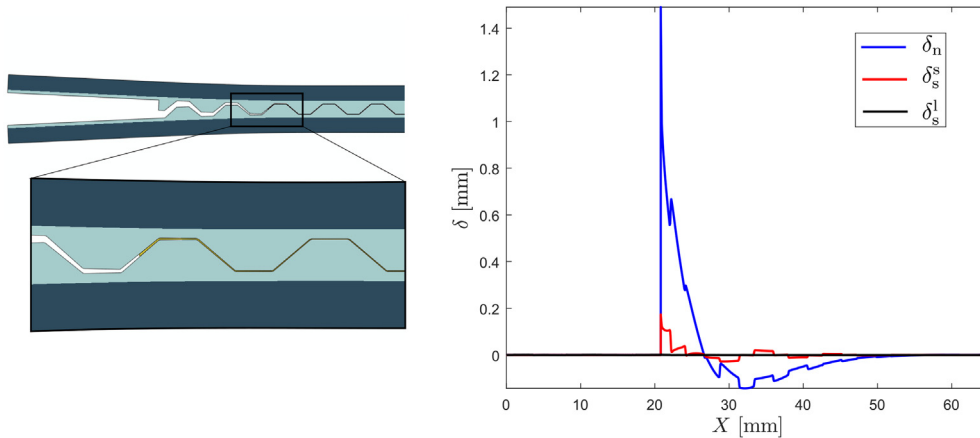


Fig. 11. Displacement profile ( $\delta_n$ ,  $\delta_s^s$ ,  $\delta_s^l$ ) along the interface at  $\Delta = 2.4$  mm and  $P/W = 2.43$  N/mm in the load–displacement curve in Fig. 12b.

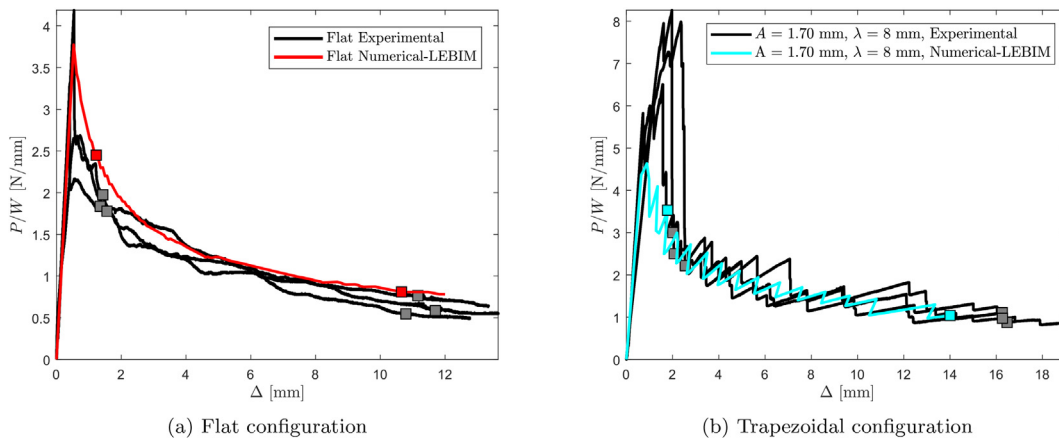
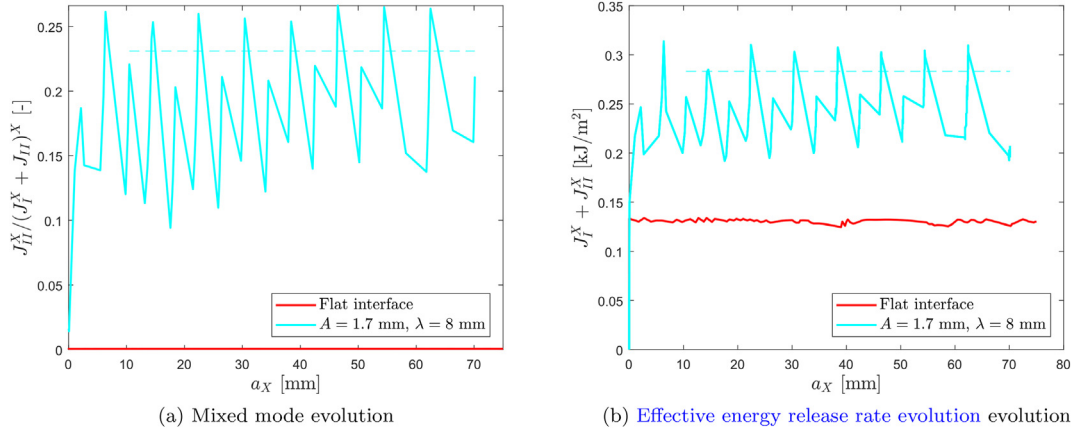


Fig. 12. Experimental–numerical correlation of the load–displacement curves. Square markers represent the points of the curves where the effective crack length reaches  $a_{X1} = 10$  mm and  $a_{X2} = 70$  mm.



**Fig. 13.** (a) Numerical evolution of the mixed mode  $J_{II}^X/J_I^X$  and (b) effective energy release rate  $J^X$  with respect to the effective crack length  $a_X$  in flat and trapezoidal configurations. Dashed lines represent the average value according to the maximum values or peaks of the curves.

**Table 7**

Critical energy release rate  $G_c^{LD}$  obtained from load–displacement curves (experimental and numerical), mean effective J-Integral  $\bar{J}_c^X$  and mean mixed mode of the flat and trapezoidal interfaces in the DCB tests.

Configuration	$G_c^{LD}$ [J/m <sup>2</sup> ] (Experimental)	$G_c^{LD}$ [J/m <sup>2</sup> ] (Numerical)	$\bar{J}_c^X$ [J/m <sup>2</sup> ]	$\frac{\bar{J}_c^X}{G_c^{LD}}$ [–]
Flat	136.3	148.7	130.3	0.0
Trapezoidal	274.0	257.6	243.3	0.231

computational curves at the beginning of the test. Then, if the crack length  $a_{X1}$  were to be selected so that the corresponding point in the load–displacement curve was located at  $\Delta \geq 4$  mm, for example, the discrepancy in the fracture toughness will be reduced. On the contrary, the average value of  $J^X$  is lower than  $G_{Ic}$ . This reduced value of the pure Mode I energy is associated with the distribution of stresses along the interface. The value of normal traction  $t_n$  just before the crack propagation is lower than the cut-off traction  $t_n^c$  established in the TSL, as depicted in Fig. 14. Hence, the critical energy release rate calculated from the J-Integral,  $\bar{J}_c^X$ , would be equal to  $G_{Ic}$  when the increments of the simulations allow an accurate/perfect traction distribution of the TSL along the interface.

Regarding the patterned configuration, the calculation of the effective fracture toughness is in close agreement: less than 7% of differ-

ence using the load–displacement curves ( $G_c^{LD}$ ) and less than 12% using the J-Integral approach ( $\bar{J}_c^X$ ). Moreover, the mixed mode based on Benzeggah-Kenane criterion is highly accurate for energy predictions:  $G_c(B = 0.231) = 245.4$  kJ/m<sup>2</sup>, see Eq. (20).

#### 4.2. Application: Hierarchical trapezoidal interfaces

Double Cantilever Beam tests including a non flat interface between adherents is performed in this Section. This kind of analysis allows the fracture energy to be studied in presence of mixed mode conditions. Furthermore, authors in Ref. [37] have demonstrated the significance of the failure modes in epoxy adhesives, which can be modelled assuming brittle behaviour. In this way, LEBIM represents an appropriate tool to describe the crack resistance in these experiments. In addition, the performance of hierarchical crack paths, involving uni-trapezoidal, bi-trapezoidal and tri-trapezoidal patterns, is herewith carried out for comparison purposes. The specimens, depicted in Fig. 15, are 160 mm in length  $L_{hier}$ , 20 mm in width  $W$  and a total height  $h$  of 4.9 mm, where nylon and glass fibre composite (GFC) are used. The bulk part of the coupon consists of 1 mm of GFC and 0.5 mm of nylon, while the layers that form the trapezoidal interface ( $A = 1.9$  mm,  $\lambda = 8$  mm) are made of nylon exclusively.

Regarding the hierarchically-based study, three orders of arrangement are investigated in the sequel: uni-trapezoidal, bi-trapezoidal and tri-trapezoidal patterns. Fig. 16 depicts the geometry definition and the differences between shapes. Pointedly, elemental features remain constant: amplitude  $A$ , wavelength  $\lambda$ , angle  $\alpha$ , horizontal length  $l_h$  and inclined length  $l_i$ . Generally speaking, the height  $A$  is reached through one, two or three jumps or steps by travelling the same distance in the horizontal axis. Particular geometrical values of the hierarchical profiles can be observed in Table 8.

For the FE analysis, 4-node plane-strain elements (type CPE4 in ABAQUS® library) are used in the GFC, the nylon and the adhesive 2D modelling. Approximately 270k elements are employed to discretize the adherents and about 130 elements form every trapezium

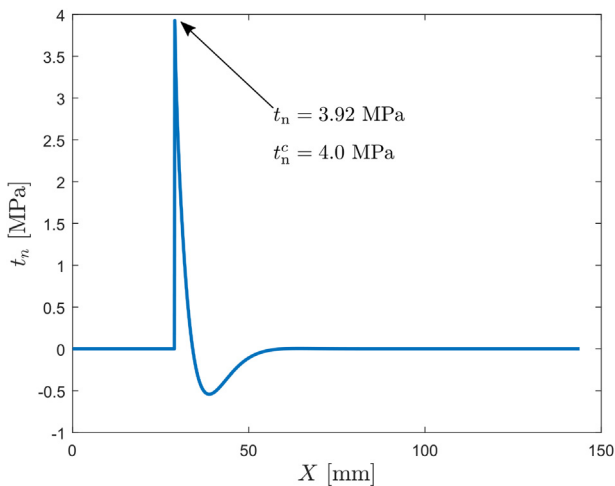


**Fig. 14.** Traction distribution along the interface corresponding to  $\Delta = 3.25$  mm and  $P/W = 1.50$  N/mm in the flat DCB test (Fig. 12).

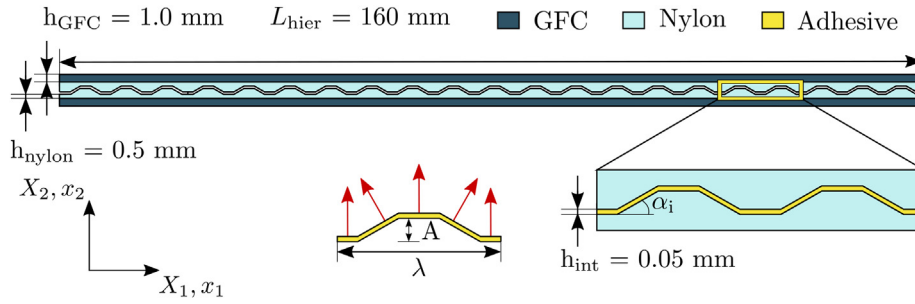


Fig. 15. Double Cantilever Beam specimen with a trapezoidal interface. Materials: glass-fibre composite (GFC), nylon and adhesive. Dimensions: length  $L_{hier}$ , height of glass-fibre composite  $h_{GFC}$ , height of nylon in the bulk part  $h_{nylon}$ , amplitude  $A$  and wavelength  $\lambda$  of the trapezoidal interface.

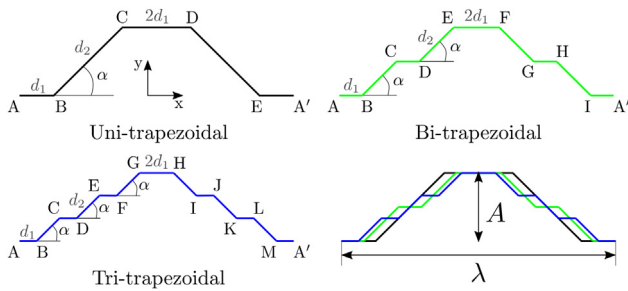


Fig. 16. Uni-trapezoidal, bi-trapezoidal and tri-trapezoidal shapes contained in the study.  $d_1$  and  $d_2$  represent the flat and inclined section length, respectively.  $\alpha$  shows the angle in the inclined sections and  $A$  and  $\lambda$  symbolise the amplitude and the wavelength of each configuration.

of the adhesive. Red arrows in Fig. 15 represent the normal direction corresponding to each section of the motif.

The same boundary conditions than those used in previous Section are applied to the current DCB-like tests: a vertical displacement at the upper left end of the specimen while the lower left end is pinned. Likewise, the control algorithm of Section 2.3 is employed in the simulations.

Considering previous aspects, numerical load–displacement curves of the uni-trapezoidal, bi-trapezoidal and tri-trapezoidal interface patterns, as well as the flat baseline scenario, can be observed in Fig. 17.

The behaviours of the three structured configurations are similar to each other being characterized by: a first linear-elastic stage before damage onset and a region characterised by pronounced instabilities in the crack advance phase. Notwithstanding, a slight increase in the maximum load of the peaks can be appreciated with the hierarchical level. Additionally, the reference case presents unstable crack propagation despite of the flat interface, which leads to a saw-tooth force–displacement curve. It is worth mentioning that, if standard displacement control boundary conditions are applied, stabilization mechanisms of the solution would be required in order to achieved equilibrium solutions throughout the simulations. Nonetheless, the control algorithm discussed above allows the computational convergence of the problem precluding the use of any artificial damping energy.

Table 8

Horizontal section length  $d_1$ , total horizontal and inclined section length,  $l_h$  and  $l_i$  respectively, and angle of the sloped sections  $\alpha$  in trapezoidal, bi-trapezoidal and tri-trapezoidal configurations.  $d_2^x$  stands for the horizontal component of the length  $d_2$ .

Configuration	$d_1$ [mm]	$d_2^x$ [mm]	$\alpha$ [rad]	$l_h$ [mm]	$l_i$ [mm]
Trapezoidal	$\frac{\lambda - 2d_2^x}{4}$	$\frac{A}{\tan \alpha}$	$\arctan \frac{4A}{\lambda}$	$\lambda/2$	$2\sqrt{(d_2^x)^2 + A^2}$
Bi-trapezoidal	$\frac{\lambda - 4d_2^x}{6}$	$\frac{A/2}{\tan \alpha}$	$\arctan \frac{4A}{\lambda}$	$\lambda/2$	$4\sqrt{(d_2^x)^2 + (A/2)^2}$
Tri-trapezoidal	$\frac{\lambda - 6d_2^x}{8}$	$\frac{A/3}{\tan \alpha}$	$\arctan \frac{4A}{\lambda}$	$\lambda/2$	$6\sqrt{(d_2^x)^2 + (A/3)^2}$

With reference to the qualitative response, the instabilities aforementioned can be also appreciated in Fig. 18, where the effective J-Integral  $J^X$ , according to Eq. (27), is represented as a function of the effective crack length  $a_x$ . In such graph, it is shown that the variability of the energy release rate is noticeable and the increase of the average fracture toughness (represented by the dashed lines and calculated by means of the peaks values) with respect to the level of arrangement. In this way, the tri-trapezoidal configuration achieves around 20% of improvement with respect to the uni-trapezoidal interface and around 83% with respect to the flat scenario.

Regarding the fracture mixed mode of the three configurations, we can observe in Fig. 19 the characteristic variability of the patterned interfaces, where the fluctuations become higher with the level of arrangement. That is, the tri-trapezoidal profile presents the highest variation of  $J_{II}^X/J_T^X$ . Furthermore, a minor increasing tendency of the mean value of the mixed mode during the test can be appreciated:  $\frac{J_{II}^X}{J_T^X}|_{mean}^{Uni} = 0.07$ ,  $\frac{J_{II}^X}{J_T^X}|_{mean}^{Bi} = 0.10$  and  $\frac{J_{II}^X}{J_T^X}|_{mean}^{Tri} = 0.11$ .

Table 9 outlines the principal fracture energy values  $G_c^{LD}$ ,  $\bar{J}_c^X$  and the mean mixed mode  $\frac{J_{II}^X}{J_T^X}|_{mean}$  during the DCB test. The use of LEBIM to characterise the behaviour of the structured interfaces facilitates the comparison of the results determined from load–displacement and J-Integral methods. Such values differ between 8.4% and 17.2%. This difference arises from the energy calculation procedure: on the one hand, the area method implicitly implies an average of every point of the load–displacement curve (between the two crack lengths selected  $a_{x1}$  and  $a_{x2}$ ); on the other hand, the J-Integral average value is performed involving the peaks of the curve in Fig. 18. The mean critical energy release rate ( $G_c^{LD}$  or  $\bar{J}_c^X$ ) increases with the level of arrangement, although such increment is small in comparison with the presence of the actual patterned interface. That is, with respect to the reference scenario (DCB test with flat interface,  $G_{ic}$ ), the simplest trapezoidal pattern implies an increment of the fracture toughness of around 56%, whereas the trapezoidal profile with the highest level of arrangement (tri-trapezoidal), involves an increase of 84%. Despite the impact of the hierarchical arrangement on the fracture properties being lower than the overall dimensions of the pattern (amplitude and wavelength), the trend suggests that increasing the arrangement

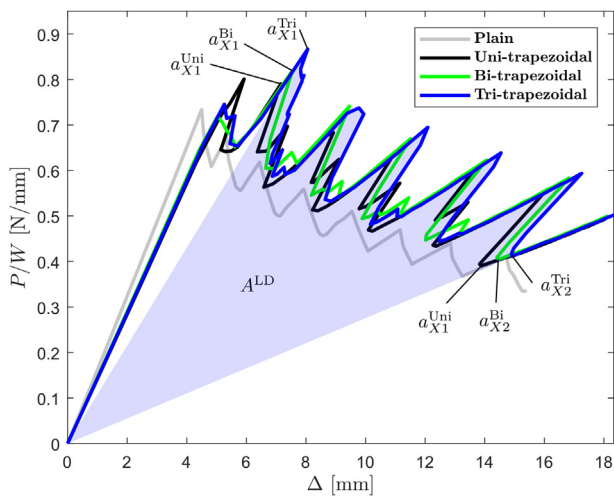


**Fig. 17.** Load vs displacement curves of DCB tests with uni-trapezoidal, bi-trapezoidal and tri-trapezoidal interface profiles.  $a_{X1}$  and  $a_{X2}$  symbolise the initial and final lengths involved in the fracture characterisation and the shaded area  $A^{LD}$  represents the area under the load–displacement curve used in Eq. (26).

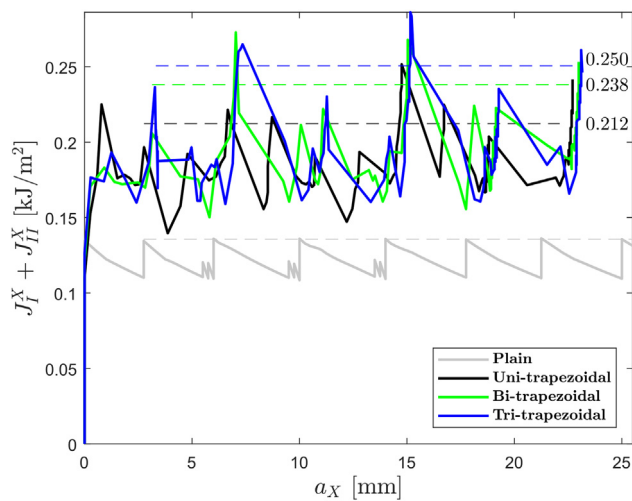


**Fig. 18.** Effective J-Integral  $J^X$  as a function of the effective crack length  $\alpha_X$  corresponding to the Double Cantilever Beam test with uni-, bi- and tri-trapezoidal crack paths.

level of the geometry may be an interesting strategy to enhance the resistance of adhesively bonded joints.

**5. Conclusions**

A comprehensive framework of computational interface modelling has been presented. The following three techniques have been summarised with the aim of overcoming difficulties during the analysis of interfaces with complex geometry: (i) an innovative versatile model to calculate interface gaps under large displacement conditions, (ii) the Linear Elastic Brittle Interface Model, able to describe the abrupt failure phenomena present in some joints, (iii) and a control algorithm to deal with instabilities that result from the fracture mixed-mode variability along non-flat interface patterns. The first two methods have been embedded in a material user-subroutine UMAT of the software package ABAQUS® whereas the latter one was performed by linking the applied boundary conditions with the crack tip opening by employing auxiliary elements.

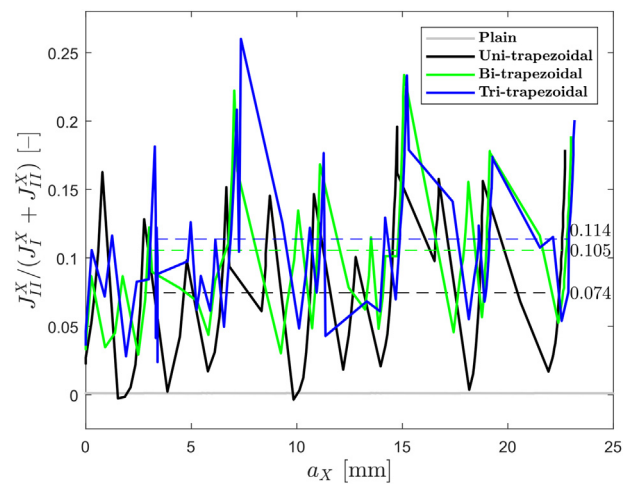


**Fig. 19.** Effective mixed mode evolution  $J_{II}^X/J_I^X$  at the crack tip as a function of the effective crack length  $\alpha_X$  corresponding to the Double Cantilever Beam test with uni-, bi- and tri-trapezoidal crack paths.

**Table 9**

Energy release rate  $G_c^{LD}$  obtained from load–displacement curves, mean effective J-Integral  $\bar{J}_c^X$  and mean mixed mode  $\frac{J_{II}^X}{J_I^X}|_{mean}$  of the hierarchical trapezoidal interfaces in the DCB tests.

Configuration	$G_c^{LD}$ [J/m <sup>2</sup> ]	$\bar{J}_c^X$ [J/m <sup>2</sup> ]	$\frac{J_{II}^X}{J_I^X} _{mean}$ [-]
Uni-trapezoidal	195.9	212.3	0.074
Bi-trapezoidal	205.1	238.1	0.105
Tri-trapezoidal	210.5	250.5	0.114

The aforementioned scheme was applied to delamination of composite laminates in a large range of mixed-mode fracture conditions: Double Cantilever Beam (DCB), Mixed Mode Bending (MMB) and End Notch Flexure (ENF) tests. Numerical results obtained from the Finite Element analysis were compared with experimental tests available in the literature. The numerical-experimental correlation exhibits an excellent agreement and the employment of this interface modelling in structures involving a large variety of mixed-mode fracture conditions is justified.

The strategy proposed was exploited in structured interface DCB Finite Element tests with different orders of hierarchical organization. In particular, uni-trapezoidal, bi-trapezoidal and tri-trapezoidal profiles were examined in the simulations. The load–displacement curves present analogous behaviours, developing a linear-elastic phase before the onset of damage and consecutive saw-tooth responses during crack propagation. It is worth mentioning that, the higher the order of the arrangement in the pattern, the larger the fluctuations and maximum peak values obtained. As load–displacement curves anticipate, energy release rate does not rely strongly on the hierarchical order for the scenarios and the geometrical parameters used in this work. Then, a higher level of hierarchical arrangement may be needed to achieve a noticeable improvement in the interface fracture properties. Additionally, the shape and overall dimensions of the pattern may have more influence than the arrangement level.

The improvement of the present model can lead to interesting future research lines:

- LEBIM can be used with several damage criteria as described in Ref. [29]. Recently, Hutchinson and Suo and Quadratic criteria were used in a LEBIM implementation together with the Coupled Criterion of Finite Fracture Mechanics for the study of the fibre–matrix interface behaviour in Ref. [49]. The results obtained were similar

to each other for both criteria. The investigation of different damage criterion of interfaces (Hutchinson-Suo, power laws, etc) using LEBIM may widen the applicability of this tool in distinct scenarios, where differences on the mode mixity and the shape of the damaged area along the interface will appear.

- The extension of this model to 3D applications in order to address interlaminar damage in intricate geometries.
- LEBIM could be compatible with fatigue behaviour or other environmental factors. Specifically, delamination of composite laminates were previously studied using a continuous distribution of linear elastic springs under cyclic loads [50,51], so that LEBIM can be an appropriate tool to describe these type of events. Moreover, the standpoint developed herein for modelling the interface behaviour under finite strains can be combined with progressive damage theories so as to analyse fatigue loading under mixed mode conditions [52], as those presented in Refs. [53,54]. Such investigations analyse the case of fatigue using elastic interfaces and/or Cohesive Zone Models. Moreover, the implementation of the LEBIM as user-defined element would enable integration of additional features within the interface element, such as fatigue [55].
- The framework developed herein can be employed to model the behaviour of short fiber reinforced composites (SFRCS) at different scales of observation [56–59], being a matter that requires comprehensive investigation activities.

## Acknowledgements

This study was supported by the Spanish Ministry of Science, Innovation and Universities and European Regional Development Fund (Project PGC2018-099197-B-I00), the Consejería de Economía y Conocimiento de the Junta de Andalucía (Spain) and Programa Operativo FEDER Andalucía 2014–2020 for financial support under the contracts US-1265577, US-1266016 and AT17-5908-USE (Acciones de transferencia del conocimiento).

## Appendix A. Supplementary data

Supplementary data associated with this article can be found, in the online version, at <https://doi.org/10.1016/j.compstruct.2020.112495>.

## References

- [1] Turon A, Camanho P, Costa J, Dávila C. A damage model for the simulation of delamination in advanced composites under variable-mode loading. *Mech Mater* 2006;38(11):1072–89.
- [2] Camanho G, Dávila C, de Moura M. Numerical simulation of mixed-mode progressive delamination in composite materials. *J Compos Mater* 2003;37:1415–38.
- [3] Távora L, Reinoso J, Blázquez A, Mantič V. On the 3d extension of failure models for adhesive joints under mixed-mode fracture conditions: Lebim and czm. *Theor Appl Fract Mech* 2019;100:362–76.
- [4] Távora L, Mantič V, Graciani E, París F. Bem analysis of crack onset and propagation along fiber–matrix interface under transverse tension using a linear elastic–brittle interface model. *Eng Anal Bound Elem* 2011;35(2):207–22 [Special issue on the advances in mesh reduction methods – In honor of Professor Subrata Mukherjee on the occasion of his 65th birthday].
- [5] Zumaquero P, Correa E, Justo J, París F. Microscopical observations of interface cracks from inter-fibre failure under compression in composite laminates. *Compos Part A Appl Sci Manuf* 2018;110:76–83.
- [6] Banea MD, da Silva LFM. Adhesively bonded joints in composite materials: an overview. *Proc Inst Mech Eng Part L J Mater Des Appl* 2009;223(1):1–18.
- [7] Reinoso J, Blázquez A, Távora L, París F, Arellano C. Damage tolerance of composite runout panels under tensile loading. *Compos Part B Eng* 2016;96:79–93.
- [8] Griffith AA. The phenomena of rupture and flow in solids. *Philos Trans R Soc Lond Ser A Contain Papers Math Phys Charact* 1921;221:163–98.
- [9] Irwin G. Analysis of stresses and strains near the end of a crack traversing a plate. *J Appl Mech* 1957;24:361–4.
- [10] Hutchinson J, Suo Z. Mixed mode cracking in layered materials. *Advances in Applied Mechanics*, vol. 29. Elsevier; 1991, p. 63–191.
- [11] Barroso A, Mantič V, París F. Singularity analysis of anisotropic multimaterial corners. *Int J Fract* 2003;119(1):1–23.
- [12] Barroso A, Mantič V, París F. Singularity parameter determination in adhesively bonded lap joints for use in failure criteria. *Compos Sci Technol* 2008;68(13):2671–7 [Directions in Damage and Durability of Composite Materials, with regular papers].
- [13] Xu JQ, Liu YH, Wang XG. Numerical methods for the determination of multiple stress singularities and related stress intensity coefficients. *Eng Fract Mech* 1999;63(6):775–90.
- [14] Groth H. Stress singularities and fracture at interface corners in bonded joints. *Int J Adhes Adhes* 1988;8(2):107–13.
- [15] Rice J. A path independent integral and the approximate analysis of strain concentration by notched and cracks. *J Appl Mech* 1968;35:379–86.
- [16] Reinoso J, Paggi M. A consistent interface element formulation for geometrical and material nonlinearities. *Comput Mech* 2014;54(6):1569–81.
- [17] Barenblatt G. The mathematical theory of equilibrium cracks in brittle fracture. *Adv Appl Mech* 1962;7:55–129.
- [18] Dugdale D. Yielding of steel sheets containing slits. *J Mech Phys Solids* 1960;8:100–4.
- [19] Reinoso J, Paggi M, Blázquez A. A nonlinear finite thickness cohesive interface element for modeling delamination in fibre-reinforced composite laminates. *Compos Part B Eng* 2017;109:116–28.
- [20] Gasser T, Ogden R, Holzapfel G. Hyperelastic modelling of arterial layers with distributed collagen fibre orientations. *J R Soc Interface* 2006;3(6):15–35.
- [21] Wang J. Investigating some technical issues on cohesive zone modeling of fracture. *J Eng Mater Technol* 2012;135:011003.
- [22] Geubelle PH, B aylor JS. Impact-induced delamination of composites: a 2d simulation. *Compos Part B Eng* 1998;29(5):589–602.
- [23] Tvergaard V, Hutchinson JW. The influence of plasticity on mixed mode interface toughness. *J Mech Phys Solids* 1993;41(6):1119–35.
- [24] Ortiz M, Pandolfi A. Finite-deformation irreversible cohesive elements for three-dimensional crack-propagation analysis. *Int J Numer Methods Eng* 1999;44(9):1267–82.
- [25] Sørensen BF, Jacobsen TK. Determination of cohesive laws by the j integral approach. *Eng Fract Mech* 2003;70(14):1841–58 [Cohesive Models].
- [26] Maloney K, Fleck N. Tear resistance of a square-wave joint: Experiment versus cohesive zone model. *International Journal of Adhesion and Adhesives* 2018;84:9–17. URL <http://www.sciencedirect.com/science/article/pii/S0143749618300356>.
- [27] Prandtl L, Knauss WG. A thought model for the fracture of brittle solids. *Int J Fract* 2011;171(2):105–9.
- [28] Mott N. Fracture of metals: theoretical considerations. *Engineering* 1948;165(14):16–8.
- [29] Mantič V, Távora L, Blázquez A, Graciani E, París F. A linear elastic–brittle interface model: application for the onset and propagation of a fibre–matrix interface crack under biaxial transverse loads. *Int J Fract* 2015;195(1–2):15–38.
- [30] Távora L, Mantič V. Crack paths formed by multiple debonds in lfrp composites. *Mech Res Commun* 2017;84:148–54.
- [31] Reinoso J, Catalanotti G, Blázquez A, Areias P, Camanho P, París F. A consistent anisotropic damage model for laminated fiber-reinforced composites using the 3d-version of the puck failure criterion. *Int J Solids Struct* 2017;126–127:37–53.
- [32] Paggi M, Reinoso J. An anisotropic large displacement cohesive zone model for fibrillar and crazing interfaces. *Int J Solids Struct* 2015;69:106–20.
- [33] Qiu Y, Crisfield M, Alfano G. An interface element formulation for the simulation of delamination with buckling. *Eng Fract Mech* 2001;68(16):1755–76.
- [34] Paggi M, Reinoso J. An anisotropic large displacement cohesive zone model for fibrillar and crazing interfaces. *Int J Solids Struct* 2015;69–70:106–20.
- [35] García-Guzmán L, Távora L, Reinoso J, París F. A consistent finite displacement and rotation formulation of the linear elastic brittle interface model for triggering interlaminar damage in fiber-reinforced composites. *Theor Appl Fract Mech* 2020. <https://doi.org/10.1016/j.tafmec.2020.102644>.
- [36] García-Guzmán L, Távora L, Reinoso J, París F. Fracture energy characterisation of a structured interface by means of a novel j-integral procedure. *J Strain Anal Eng Des* 2019;54(7–8):364–78.
- [37] García-Guzmán L, Távora L, Reinoso J, Justo J, París F. Fracture resistance of 3d printed adhesively bonded dcb composite specimens using structured interfaces: Experimental and theoretical study. *Compos Struct* 2018;188:173–84.
- [38] ABAQUS/Standard User's Manual, Version 6.14. Simulia; 2014.
- [39] Bonet J, Wood RD. *Nonlinear continuum mechanics for finite element analysis*. 2nd ed. Cambridge University Press; 2008. doi: 10.1017/CBO9780511755446.
- [40] Benzeggagh M, Kenane M. Measurement of mixed-mode delamination fracture toughness of unidirectional glass/epoxy composites with mixed-mode bending apparatus. *Compos Sci Technol* 1996;56(4):439–49.
- [41] Camanho PP, Davila CG, de Moura MF. Numerical simulation of mixed-mode progressive delamination in composite materials. *J Compos Mater* 2003;37(16):1415–38.
- [42] Riks E. An incremental approach to the solution of snapping and buckling problems. *Int J Solids Struct* 1979;15(7):529–51.
- [43] Tvergaard V. Effect of thickness inhomogeneities in internally pressurized elastic-plastic spherical shells. *J Mech Phys Solids* 1976;24(5):291–304.
- [44] Segurado J, Llorca J. A new three-dimensional interface finite element to simulate fracture in composites. *Int J Solids Struct* 2004;41(11):2977–93.
- [45] Martínez-Pañeda E, del Busto S, Betegón C. Non-local plasticity effects on notch fracture mechanics. *Theor Appl Fract Mech* 2017;92:276–87.
- [46] Juul K, Martínez-Pañeda E, Nielsen K, Niordson C. Steady-state fracture toughness of elastic-plastic solids: Isotropic versus kinematic hardening. *Eng Fract Mech* 2019;207:254–68.

- [47] Reeder JR, Rews JH. Mixed-mode bending method for delamination testing. *AIAA J* 1990;28(7):1270–6.
- [48] Airbus. Carbon Fibre Reinforced Plastics. Determination of fracture toughness energy of bonded joints. Mode I. G1C. Issue 1. AITM 1-0053; 2006.
- [49] Muñoz-Reja M, Távora L, Mantić V, Cornetti P. Crack onset and propagation at fibre–matrix elastic interfaces under biaxial loading using finite fracture mechanics. *Compos Part A Appl Sci Manuf* 2016;82:267–78.
- [50] Bennati S, Valvo P. Delamination growth in composite plates under compressive fatigue loads. *Compos Sci Technol* 2006;66(2):248–54.
- [51] Bennati S, Fusicaro P, Valvo PS. An elastic-interface model for the mixed-mode bending test under cyclic loads. *Procedia Struct Integr* 2016;2:72–9.
- [52] Zhang J, Li HY, Li H, Jia H. Investigation on fatigue performance of adhesively bonded butt-joints and multiaxial life estimation using stress-based failure models. *Theor Appl Fract Mech* 2020;107:102498.
- [53] Hosseini-Toudeshky H, Sheibanian F, Ovesy HR, Goodarzi MS. Prediction of interlaminar fatigue damages in adhesively bonded joints using mixed-mode strain based cohesive zone modeling. *Theor Appl Fract Mech* 2020;106:102480.
- [54] Rocha A, Akhavan-Safar A, Carbas R, Marques E, Goyal R, El-zein M, et al. Numerical analysis of mixed-mode fatigue crack growth of adhesive joints using CZM. *Theor Appl Fract Mech* 2020;106:102493.
- [55] del Busto S, Betegón C, Martínez-Pañeda E. A cohesive zone framework for environmentally assisted fatigue. *Eng Fract Mech* 2017;185:210–26.
- [56] Dean A, Grbic N, Rolfes R, Behrens B. Macro-mechanical modeling and experimental validation of anisotropic, pressure- and temperature-dependent behavior of short fiber composites. *Compos Struct* 2019;211:630–43.
- [57] Dean A, Sahraee S, Reinoso J, Rolfes R. Finite deformation model for short fiber reinforced composites: application to hybrid metal-composite clinching joints. *Compos Struct* 2016;151:162–71.
- [58] Dean A, Reinoso J, Sahraee S, Rolfes R. An invariant-based anisotropic material model for short fiber-reinforced thermoplastics: coupled thermo-plastic formulation. *Compos Part A Appl Sci Manuf* 2016;90:186–99.
- [59] Dean A, Sahraee S, Reinoso J, Rolfes R. A new invariant-based thermo-plastic model for finite deformation analysis of short fibre reinforced composites: development and numerical aspects. *Compos Part B Eng* 2017;125:241–58.